molecules

MDPI

Article

Morphology-Controlled Synthesis of $V_{1.11}S_2$ for Electrocatalytic Hydrogen Evolution Reaction in Acid Media

Qiuyue Chen [1,2,3], Siqi Tian [2], Xiaonan Liu [1,*], Xuguang An [2], Jingxian Zhang [2], Longhan Xu [2], Weitang Yao [2] and Qingquan Kong [2,*]

[1] College of Chemical Engineering, Sichuan University of Science & Engineering, Zigong 643000, China
[2] School of Mechanical Engineering, Chengdu University, Chengdu 610106, China
[3] School of Chemical Engineering, Sichuan University, Chengdu 610065, China
* Correspondence: lxn@suse.edu.cn (X.L.); kongqingquan@cdu.edu.cn (Q.K.)

Abstract: High-performance low-cost catalysts are in high demand for the hydrogen evolution reaction (HER). In the present study, we reported that $V_{1.11}S_2$ materials with flower-like, flake-like, and porous morphologies were successfully synthesized by hydrothermal synthesis and subsequent calcination. The effects of morphology on hydrogen evolution performance were studied. Results show that flower-like $V_{1.11}S_2$ exhibits the best electrocatalytic activity for HER, achieving both high activity and preferable stability in 0.5 M H_2SO_4 solution. The main reason can be ascribed to the abundance of catalytically active sites and low charge transfer resistance.

Keywords: hydrogen evolution reaction; $V_{1.11}S_2$; morphology; hydrothermal synthesis

Citation: Chen, Q.; Tian, S.; Liu, X.; An, X.; Zhang, J.; Xu, L.; Yao, W.; Kong, Q. Morphology-Controlled Synthesis of $V_{1.11}S_2$ for Electrocatalytic Hydrogen Evolution Reaction in Acid Media. *Molecules* **2022**, *27*, 8019. https://doi.org/10.3390/molecules27228019

Academic Editor: Paolo Bertoncello

Received: 19 October 2022
Accepted: 15 November 2022
Published: 18 November 2022

1. Introduction

Nowadays, the development of green and sustainable energy has become an important research topic due to the depletion of fossil fuels, as well as increasing serious environmental issues [1,2]. Therefore, it is urgent to develop renewable and clean alternatives. Electrochemical water splitting is considered to be a clean and sustainable way to produce hydrogen fuel [3]. Moreover, the abundance of protons in acid electrolytes facilitates the acceleration of the hydrogen evolution reaction [4]. However, the acidic electrolyte can cause severe chemical corrosion of electrolyzers, which limits the use of non-platinum group metals or their compounds as catalysts [5]. In particular, the high cost and insufficient reserves of precious metals have greatly restricted their large-scale commercial applications [6,7]. Therefore, a lot of research has been focused on exploring low-cost electrocatalysts [8–12].

Among the various hydrogen evolution reaction (HER) catalysts, transition metal chalcogenides (TMDs) have made tremendous progress due to their high catalytic activity toward the HER, as well as their low-cost [13,14]. MoS_2 is one of the most excellent electrocatalytic materials among transition metal sulfides, and the catalytic activity and mechanism of MoS_2 for HER have been widely understood [15–18]. MoS_2 with a two-dimensional (2D) layered structure is known to contain both active edge sites and chemically inert basal plane. Lots of work has been conducted to improve the activity by increasing the edge sites of MoS_2 and/or exploiting the inert basal plane to create additional active sites [19,20]. Hexagonal 1T-phase VS_2 (1T-VS_2) as a group TMDs is a promising HER electrocatalyst. The structure of 1T-VS_2 is similar to that of MoS_2, which is assembled by stacked S-V-S monolayers via weak van der Waals interaction, which also has excellent structural stability. For the first time, Pan demonstrated by density functional theory calculation that the catalytic performance of single-layer VS_2 is equivalent to that of Pt at low hydrogen coverage [21]. Zhang and his colleagues further explained the role of intrinsic point defects in HER activity of monolayer VS_2 catalyst [22]. After that, Liang et al. developed a facile hydrothermal calcination method to synthesize self-supported VS_2 on carbon paper,

which shows excellent HER properties [23]. Qu and his colleagues also prepared VS_2 with flower-like morphology, obtaining superior HER performance in acid solution [24].

$V_{1.11}S_2$ phase is one of nonstoichiometric 1T-V_1 + $_X$$S_2$ (0 < X< 0.17) with V atoms in the interstitial site between adjacent layers (X is the concentration of V atoms) [25,26]. Both theoretical and experimental results indicate the excellent HER activity of self-intercalated $V_{1.11}S_2$, which shows a much faster proton/electron adsorption and hydrogen release process than the VS_2 [26]. Despite these advances, there were few reports focused on the morphology-controlled synthesis of $V_{1.11}S_2$, as well as their effect on HER performance. It is well known that electrocatalytic activities are highly reliant on the catalyst morphology, which is given more edge sites and lowly coordinated surface atoms that often determine the catalytic performance [27].

Herein, different morphologies of $V_{1.11}S_2$ were synthesized by a simple hydrothermal synthesis and subsequent calcination (Figure 1). The electrochemical catalytic properties of the resultant $V_{1.11}S_2$ materials were systematically investigated.

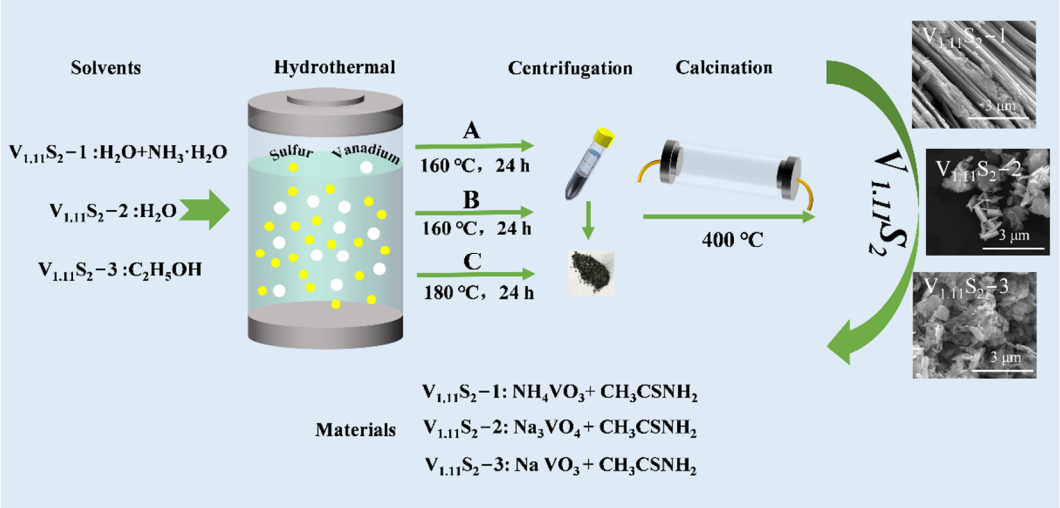

Figure 1. Schematic for the synthesis of $V_{1.11}S_2$ with different morphology.

2. Results and Discussion

Figure 2 shows the XRD patterns of the obtained $V_{1.11}S_2$ materials. All the diffraction peaks can be assigned to the $V_{1.11}S_2$ (33–1445) phase without discernible impurities. It was found that both $V_{1.11}S_2$-1 and $V_{1.11}S_2$-2 have a well-crystalline phenomenon. It can be seen from Figure 2 and Figure S1 that the XRD diffraction peaks before and after calcination are quite different, which is mainly due to the transformation of VS_4 and VS_2 to $V_{1.11}S_2$ at high-temperature conditions [28].

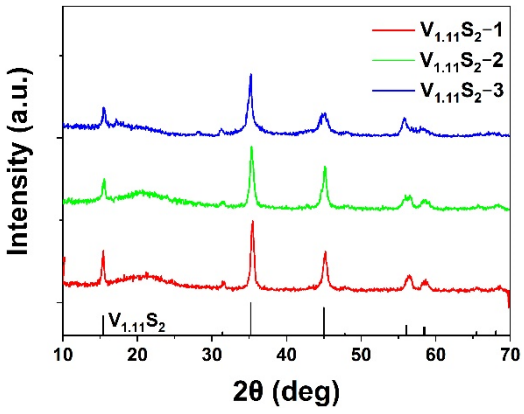

Figure 2. The XRD patterns of the as-annealed $V_{1.11}S_2$ materials.

Figure 3 shows the FE-SEM images of $V_{1.11}S_2$ materials. Figure 3a,b display that flower-like $V_{1.11}S_2$ is stacked by a large number of $V_{1.11}S_2$ nanoplates in different directions. It is worth noting that the average radius of a single $V_{1.11}S_2$ nanoflower is about 10 µm. Moreover, the formation of flowerlike $V_{1.11}S_2$ probably involves two steps [29]. First, in a weak alkaline environment, the −SH functional group produced by C_2H_5NS reacts with the precursor of V to form V-S intermediate complexes followed by decomposing to shape VSx (x = 2, 4) nuclei for further growth. Then, VSx nanoplates are transformed at high temperatures into $V_{1.11}S_2$ nanosheets, which are stacked together to form flower-like structures. Irregular flake $V_{1.11}S_2$ prepared by process B is shown in Figure 3c and Figure S2a. It can be seen from Figure S3b that the precursor obtained in process B is closely stacked by nanosheets, which are dispersed and smaller after calcination. When the solvent change to ethanol, a porous structure can be observed (Figure 3d). Compared with the powder before calcination shown in Figure S3c, the morphology changes dramatically, which is mainly due to the slight solubility of $NaVO_3$ in ethanol solution and the calcination procedure [30]. These results suggest the morphology can be easily controlled by altering the hydrothermal solvent and the source of vanadium. Transmission electron microscope (TEM) measurements were performed to analyze the physical structure of the $V_{1.11}S_2$-1. As depicted in Figure 4a, flower-like $V_{1.11}S_2$-1 can be exfoliated into a nanosheet structure under long−time ice bath ultrasound. The high-magnification TEM image shown in Figure 4b exhibits the periodic lattice fringe pattern, and the inter-planar spacing was measured to be 0.163 nm, which agrees with that of the (110) facet of $V_{1.11}S_2$ (Figure 4b). The corresponding selected area electron diffraction (SAED) pattern also confirmed the crystal structure of the $V_{1.11}S_2$ phase (inset in Figure 4b). Moreover, the EDS pattern in Figure S4 also reveals that V and S can be detected.

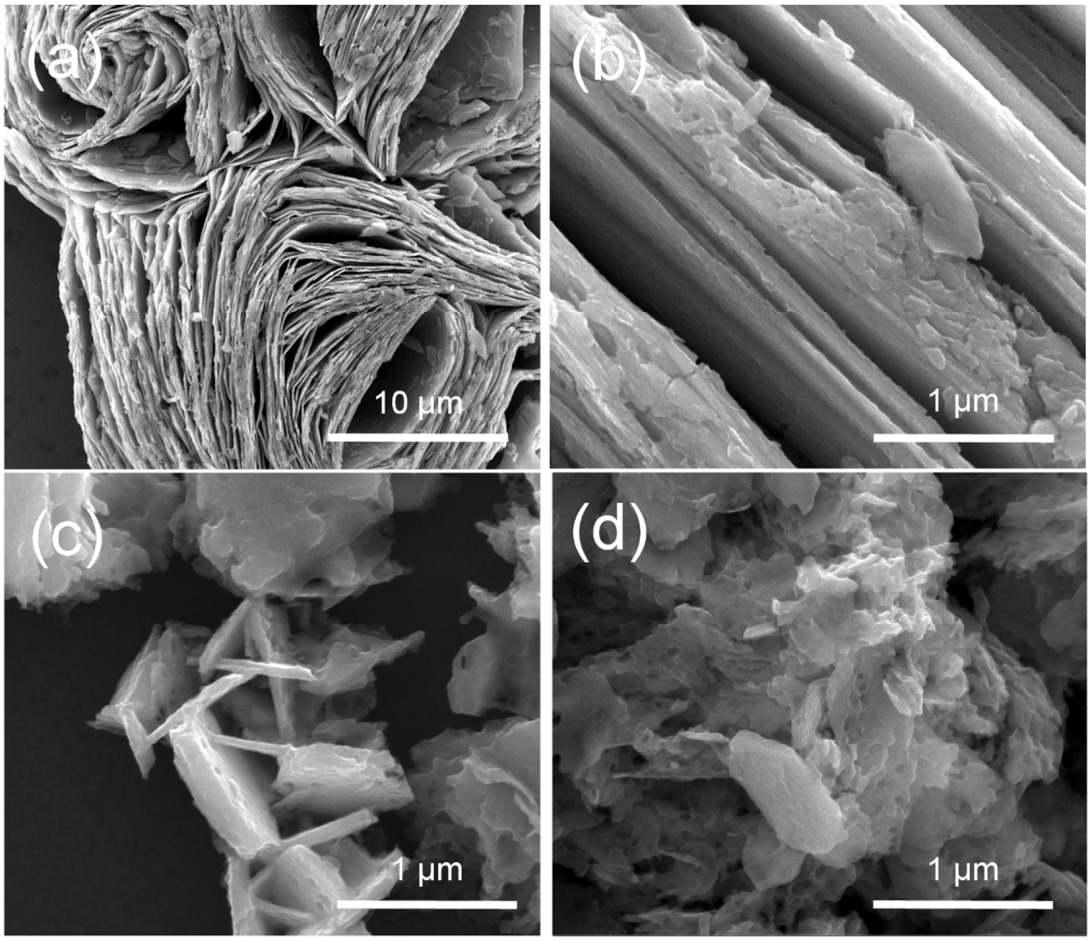

Figure 3. FE-SEM images of $V_{1.11}S_2$ materials. (**a**,**b**) $V_{1.11}S_2$-1, (**c**) $V_{1.11}S_2$-2, (**d**) $V_{1.11}S_2$-3.

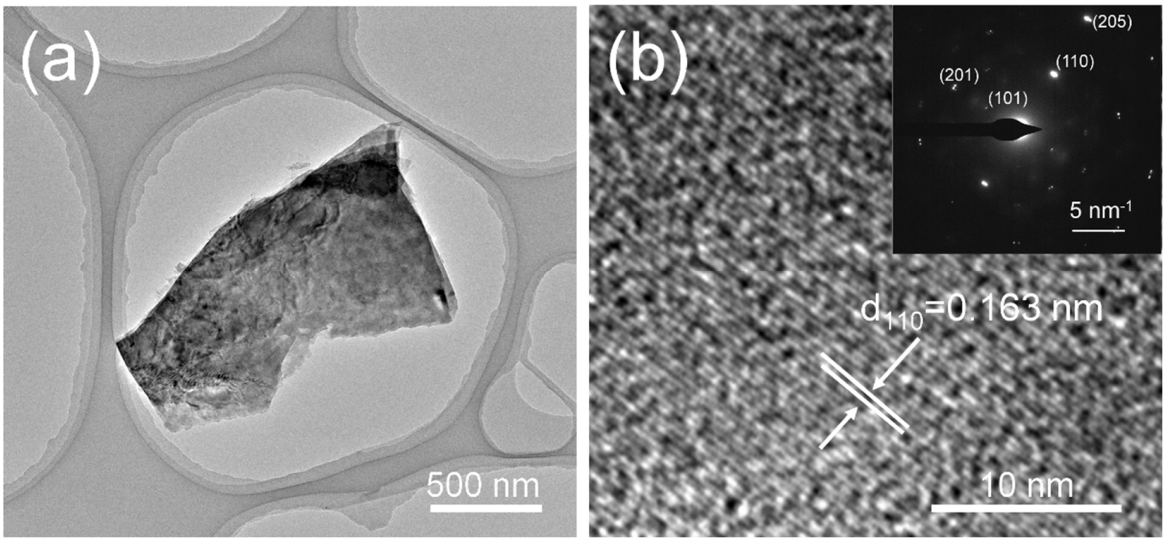

Figure 4. (**a**) TEM images, and (**b**) high-magnification TEM images of the $V_{1.11}S_2$-1 materials. The inset in Figure (**b**) is the corresponding SAED pattern.

To detect the surface chemical state and element composition, X-ray photoelectron spectroscopy (XPS) analysis was performed on $V_{1.11}S_2$ with different morphologies. Investigation of the XPS spectrum clearly shows the presence of V and S (Figure S5). The V 2p spectra can be fitted with two sets of doublet peaks (Figure 5a), and the spectrum of $V_{1.11}S_2$(V 2p) shows two additional broad peaks at a lower binding energy of 513.4, 516.3, 520.9, and 523.8 eV, which can be respectively assigned to $V^{2+}2p_{3/2}$, $V^{4+}2p_{3/2}$, $V^{2+}2p_{1/2}$, and $V^{4+}2p_{1/2}$ [26]. The peak fitting analysis of S 2p (Figure 5b) confirms the presence of S^{2-} with two peaks located at 160.8 and 162 eV that can be assigned to $S2p_{3/2}$ and $S2p_{1/2}$ [26,31]. The combined above-mentioned data indicate that the $V_{1.11}S_2$ materials with different morphologies have been successfully prepared.

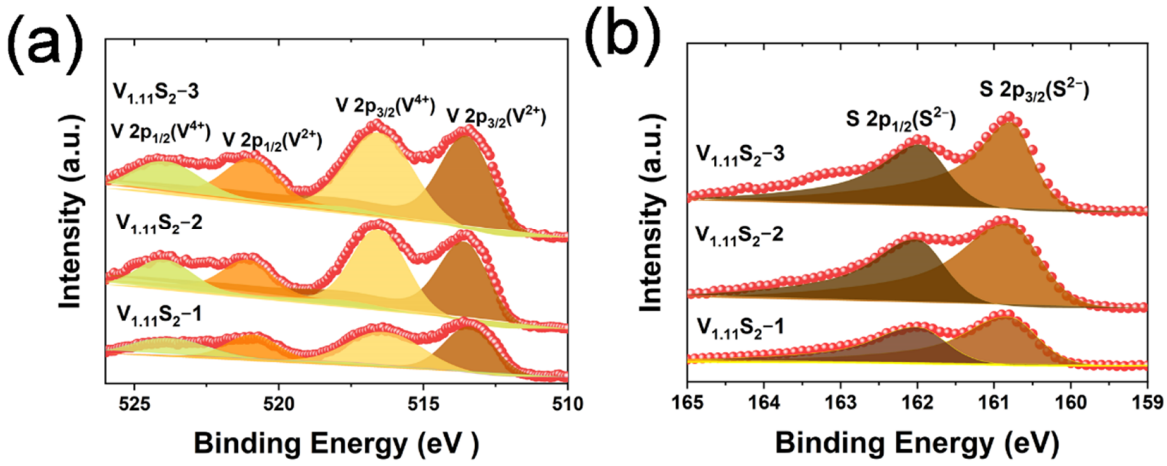

Figure 5. XPS high-resolution spectra of (**a**) V 2p and (**b**) S 2p for the $V_{1.11}S_2$-1, $V_{1.11}S_2$-2, and $V_{1.11}S_2$-3 materials.

The electrocatalytic HER activities of $V_{1.11}S_2$ materials were assessed by linear sweep voltammetry (LSV) using a three-electrode system under 0.5 M H_2SO_4 acidic aqueous condition. From Figure 6a, $V_{1.11}S_2$-1 exhibits the best catalytic performance, achieving a current density of 10 mA cm^{-2} with an overpotential of 252 mV, which is superior to the previously reported vanadium sulfide acidic HER electrocatalysts, such as VS_2 nanodiscs (420 mV) [32], CFP supported $V_{1.11}S_2$ (259.7 mV) [33], non−templated VS_2 (378 mV) [34], and Co-N-doped single-crystal V_3S_4 nanoparticles (268 mV) [35]. As illustrated in Figure 6b,

the calculated Tafel slopes of $V_{1.11}S_2$-1, $V_{1.11}S_2$-2, $V_{1.11}S_2$-3, and 5 wt.% Pt/C are 71.7 mV dec^{-1}, 264.1 mV dec^{-1}, 102.5 mV dec^{-1}, and 30.6 mV dec^{-1}, respectively. It is worth noting that the Tafel slope of 5 wt.% Pt/C is as low as 30.6 mV dec^{-1}, which is consistent with previous studies [36,37]. Therefore, $V_{1.11}S_2$-1 shows lower overpotential and Tafel slope, indicating its high HER activities.

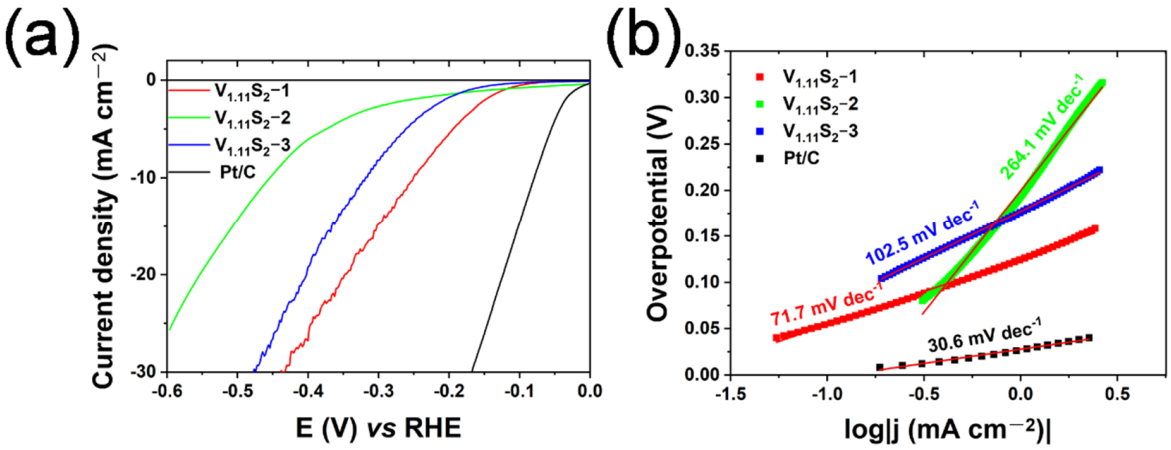

Figure 6. Electrochemical property of $V_{1.11}S_2$ materials for HER in 0.5 M H_2SO_4. (**a**) The iR-corrected polarization curves; (**b**) Tafel plots of $V_{1.11}S_2$-1, $V_{1.11}S_2$-2, $V_{1.11}S_2$-3, and 5 wt.% Pt/C.

The stability of the catalyst plays an important role in practical application. The stability test of $V_{1.11}S_2$-1 was also carried out by chronopotentiometry test. From Figure S6, the potential remains stable at the current density of 10 mA cm^{-2}. For comparison, the potential of 5 wt.% Pt/C drops dramatically with the extension of test time, which is consistent with previous studies [38,39]. After the chronopotentiometry test, the LSV curves of $V_{1.11}S_2$-1 show a negligible recession phenomenon (Figure S7), suggesting that the catalyst maintains a highly stable catalytic performance. In brief, the above electrochemical test results confirm the flower-like $V_{1.11}S_2$ material has superior electrochemical activity and stability for HER.

According to previous studies, the catalytic active H−adsorption site of the $V_{1.11}S_2$ catalyst is S in the outermost layer [24,40]. Generally, the electrocatalytic activity is highly dependent on the catalyst morphology with more active sites. In order to further clarify the origination of excellent HER performance for $V_{1.11}S_2$ materials, both the electrochemical surface area (ECSA) of the samples were tested. The corresponding current in the applied potential window of 0.06–0.16 V vs. the reversible hydrogen electrode (RHE) should be originated from the charging of the double-layer, and the calculated capacitance (C_{dl}) should be proportional to the ECSA [41]. As shown in Figure 7 and the corresponding cyclic voltammograms in Figure S8, $V_{1.11}S_2$-1 has higher electric double-layer capacitance (3.4 mF cm^{-2}) than $V_{1.11}S_2$-2 (0.45 mF cm^{-2}) and $V_{1.11}S_2$-2 (1.9 mF cm^{-2}). Moreover, the fitting value R−Squares is listed in Table S1, suggesting $V_{1.11}S_2$-1 has a larger surface area with more exposed active sites. This may be one of the reasons for its high HER performance.

EIS measurements were performed to examine the kinetic differences between $V_{1.11}S_2$ in different morphologies during the electrochemical process [42]. As shown in the illustration in Figure 8, the semicircle in the Nyquist plots was fitted by using the Randles equivalent circuit, in which Rs represents the equivalent series resistance, Rct_1 represents the charge transfer resistance of the electrode, and CPE represents the constant phase element [43,44]. It is worth noting that the charge transfer resistance (Rct_1) is related to the electrocatalytic kinetics, and a lower value corresponds to a faster reaction rate, which can be quantified from the diameter of the semicircle in the low-frequency zone [45]. Table 1 demonstrates the changing trend of the Rct_1 value for $V_{1.11}S_2$ nanomaterials with different morphologies, $V_{1.11}S_2$-1 (49.54 Ω) < $V_{1.11}S_2$-3 (60.8 Ω) < $V_{1.11}S_2$-2 (114.3 Ω), indicating that

$V_{1.11}S_2$-1 has better conductivity. Overall, we can conclude that the enhanced catalytic HER activity of flower-like $V_{1.11}S_2$ compared to the other two structures can be accountable for both the abundant catalytically active sites and preferable low charge transfer resistance.

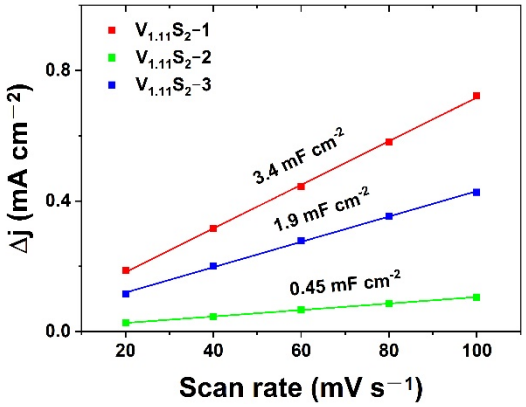

Figure 7. Estimation of Cdl by liner fitting the differences in current density variation (Ja-Jc) at 0.15 V (vs. SCE) as a function of scan rate.

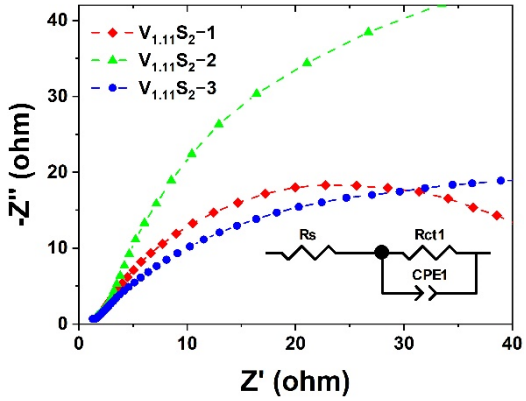

Figure 8. Nyquist plots for $V_{1.11}S_2$ materials without iR compensation.

Table 1. The electrochemical equivalent circuit (EEC) parameters of $V_{1.11}S_2$ nanomaterials with different morphologies were obtained by fitting the Nyquist diagram.

Catalyst	$V_{1.11}S_2$-1	$V_{1.11}S_2$-2	$V_{1.11}S_2$-3
Rs(Ω)	0.36 ± 0.023	0.34 ± 0.014	0.49 ± 0.021
Rct_1 (Ω)	49.54 ± 0.48	114.3 ± 3.27	60.8 ± 1.08
CPE_2-T(F)	$2.03 \times 10^{-3} \pm 7.77 \times 10^{-6}$	$1.84 \times 10^{-4} \pm 1.32 \times 10^{-5}$	$2.15 \times 10^{-3} \pm 4.84 \times 10^{-5}$
CPE_2-P(F)	$0.82 \pm 5.33 \times 10^{-3}$	0.90 ± 0.012	$0.69 \pm 3.89 \times 10^{-3}$

3. Experimental Section

3.1. Materials

Ammonium vanadate (NH_4VO_3), sodium orthovanadate ($Na_3VO_4 \cdot 12H_2O$), sodium metavanadate ($NaVO_3$), vanadyl acetylacetonate ($C_{10}H_{14}O_5V$), thioacetamide (CH_3CSNH_2), cysteine ($C_3H_7NO_2S$), ammonia ($NH_3 \cdot H_2O$), deionized water (H_2O), anhydrous ethanol (C_2H_6O), N-methyl pyrrolidone (C_5H_9NO). The above chemicals and reagents were purchased from Chengdu Kelong Co., Ltd., Chengdu, China. All reagents were used directly without further purification. The commercial 5 wt.% Pt/C catalyst was purchased from Macleans. Carbon paper (TGP-H-060) was purchased from yilongsheng Energy Technology Co., Ltd., Suzhou, China.

3.2. Synthesis of $V_{1.11}S_2$ Materials

The schematic for the synthesis of $V_{1.11}S_2$ with different morphology is shown in Figure 1. In process A, 1 mmol NH_4VO_3 and 10 mmol CH_3CSNH_2 were first dissolved in a solution containing 38 mL deionized water and 2 mL $NH_3{\cdot}H_2O$, which was stirred for 1 h to form a uniform solution. Afterward, the prepared solution was transferred to a 50 mL Teflon-lined stainless-steel autoclave and maintained at 160 °C for 24 h. After natural cooling to room temperature, the black precipitates were collected by centrifugation, washed several times with deionized water and absolute ethanol, and dried under a vacuum for 6 h. In process B, 1 mmol $NaVO_3$ was used as a vanadium source, and 15 mmol CH_3CSNH_2 as a sulfur source, dissolved in 25 mL deionized water; other reaction conditions were the same. In process C, 4 mmol $NaVO_3$, and 24 mmol CH_3CSNH_2 were dissolved in 25 mL C_2H_6O, and the reaction temperature was raised to 180 °C. All final precipitates were calcined at 400 °C for 2 h to obtain $V_{1.11}S_2$. These $V_{1.11}S_2$ materials obtained by different preparation procedures were labeled as $V_{1.11}S_2$-1, $V_{1.11}S_2$-2, and $V_{1.11}S_2$-3, respectively.

3.3. Materials Characterization

The phase constitutes of the obtained samples were characterized by an X-ray diffractometer (XRD, DX-2700B) with Cu Kα radiation. The microstructure of $V_{1.11}S_2$ with different morphology was examined by a field emission scanning electron microscope (FESEM, FEI Insect F50). The TEM images of $V_{1.11}S_2-1$ were obtained by high-resolution transmission electron microscopy (TEM, FEI Talos F200S Super). The surface valence states and elemental compositions were analyzed using X-ray photoelectron spectroscopy (XPS, Thermo Fischer, ESCALAB Xi^+).

3.4. Electrochemical Measurements

All electrochemical data were measured by an electrochemical workstation (CHI660E, CH Instrument, Shanghai, China) with a typical three-electrode electrochemical cell in the acidic electrolyte (0.5 M H_2SO_4). A graphite rod was used as the counter electrode, and a saturated calomel electrode was used as the reference electrode. The working electrode was prepared as follows: 3 mg catalysts and 50 μL Nafion solution (5 wt.%) were dispersed in 500 μL mixed solvent of deionized water−isopropanol (volume ratio of 3:1), then sonication to form a homogeneous ink solution. Ink with a volume of 15 μL was loaded onto the carbon paper (0.25 cm^{-2}) electrode and dried at ambient temperature. A loading density of about 0.343 mg cm^{-2} was obtained. Linear sweep voltammograms (LSV) were measured from 0.10 to −0.90 V (vs. RHE) at a scan rate of 5 mV s^{-1}. Electrochemical impedance spectroscopy (EIS) was conducted under −238 mV (vs. RHE) over a frequency range from 100 kHz to 0.01 Hz with a 5mV amplitude potential. The cyclic voltammograms (CV) measurements at various scan rates from 20, 40, 60, 80, and 100 mV s^{-1} were performed in the potential range of 0.06~0.16 V (vs. RHE) for the electrochemical double−layer capacitance (C_{dl}) estimation. It should be noted that no iR compensation was applied to our testing data. According to $E_{corrected} = E_{measured} - i \times R_s$, all potentials are corrected by iR, where i is the test current and Rs is the equivalent series resistance, which is determined by the Nyquist plots fitting.

4. Conclusions

In conclusion, $V_{1.11}S_2$ was successfully synthesized by hydrothermal synthesis and subsequent calcination. The morphology can be easily controlled by altering the hydrothermal solvent and the source of vanadium. The electrocatalysis results show that the flower−like $V_{1.11}S_2$ has the best catalytic activity, which can be ascribed to abundant catalytically active sites and preferable low charge transfer resistance. This research provides us with a strong basis for the morphology dependent of $V_{1.11}S_2$ materials towards HER. Further works will be performed to enhance the intrinsic activity of $V_{1.11}S_2$ and/or supported on conductive substrates such as carbon cloth and metal foam.

Supplementary Materials: The following supporting information can be downloaded at: https://www.mdpi.com/article/10.3390/molecules27228019/s1, Figure S1: XRD patterns of hydrothermal synthesis precursor powder before annealing; Figure S2: FE-SEM images of (a) $V_{1.11}S_2$-2, and (b) $V_{1.11}S_2$-3 materials; Figure S3: FE-SEM images of precursor powder before annealing, (a) $V_{1.11}S_2$-1, (b) $V_{1.11}S_2-2$, and (c) $V_{1.11}S_2$-3, respectively; Figure S4: EDS pattern of $V_{1.11}S_2-1$ materials; Figure S5: XPS survey spectra of $V_{1.11}S_2$-1, $V_{1.11}S_2$-2, and $V_{1.11}S_2$-3 materials; Figure S6: Chronopotentiometry curve of $V_{1.11}S_2$-1 and Pt/C recorded at the current density of 10 mA cm^{-2} for a total duration of 5 h; Figure S7: Initial (red line) and after 5 h (purple line) polarization curves of $V_{1.11}S_2$-1 material; Figure S8: Voltammograms of (a) $V_{1.11}S_2$-1, (b) $V_{1.11}S_2$-2 and (c) $V_{1.11}S_2$-3 at various scan rates of 20, 40, 60, 80 and 100 mV s^{-1}, respectively; Table S1: the electric double layer (Cdl) capacitance is obtained by fitting CV curve.

Author Contributions: Methodology, X.L. and W.Y.; Software, X.A., J.Z. and L.X.; Formal analysis, Q.K.; Data curation, Q.C. and S.T. All authors have read and agreed to the published version of the manuscript.

Funding: This research was funded by the National Natural Science Foundation of Qingquan Kong grant number: 11832007. This research was funded by the Application and Foundation Research Projects of Qingquan Kong grant number: 2022NSFSC1965, 2022JDRC0085. This research was funded by the Wuliangye Group Industry University Research Cooperation Project of Xiaonan Liu grant number: CXY2021ZR002.

Informed Consent Statement: Not applicable.

Data Availability Statement: The data presented in this study are available on request from the corresponding author. The data are not publicly available due to restrictions eg privacy or ethical.

Acknowledgments: Many thanks go to Chenghua Sun from the Swinburne University of Technology who provided discussions and good suggestions.

Conflicts of Interest: The authors declare no conflict of interest.

References

1. Zhou, W.; Jia, J.; Lu, J.; Yang, L.; Hou, D.; Li, G.; Chen, S. Recent developments of carbon−based electrocatalysts for hydrogen evolution reaction. *Nano Energy* **2016**, *28*, 29–43. [CrossRef]
2. Chen, Z.; Duan, X.; Wei, W.; Wang, S.; Ni, B.J. Recent advances in transition metal−based electrocatalysts for alkaline hydrogen evolution. *J. Mater. Chem. A* **2019**, *7*, 14971–15005. [CrossRef]
3. Zhu, J.; Hu, L.; Zhao, P.; Lee, L.Y.S.; Wong, K.Y. Recent Advances in Electrocatalytic Hydrogen Evolution Using Nanoparticles. *Chem. Rev.* **2020**, *120*, 851–918. [CrossRef]
4. Hu, K.; Ohto, T.; Nagata, Y.; Wakisaka, M.; Aoki, Y.; Fujita, J.I.; Ito, Y. Catalytic activity of graphene-covered non-noble metals governed by proton penetration in electrochemical hydrogen evolution reaction. *Nat. Commun.* **2021**, *12*, 203. [CrossRef]
5. Yang, C.; Zhao, R.; Xiang, H.; Wu, J.; Zhong, W.; Li, W.; Zhang, Q.; Yang, N.; Li, X. Ni-Activated Transition Metal Carbides for Efficient Hydrogen Evolution in Acidic and Alkaline Solutions. *Adv. Energy Mater.* **2020**, *10*, 2002260. [CrossRef]
6. Li, Y.; Wei, X.; Chen, L.; Shi, J. Electrocatalytic Hydrogen Production Trilogy. *Angew. Chem. Int. Ed. Engl.* **2020**, *10*, 1–21.
7. Du, H.; Kong, R.M.; Guo, X.; Qu, F.; Li, J. Recent progress in transition metal phosphides with enhanced electrocatalysis for hydrogen evolution. *Nanoscale* **2018**, *10*, 21617–21624. [CrossRef]
8. Wang, C.; Tian, B.; Wu, M.; Wang, J. Revelation of the Excellent Intrinsic Activity of MoS_2 | NiS | MoO_3 Nanowires for Hydrogen Evolution Reaction in Alkaline Medium. *ACS Appl. Mater. Inter.* **2017**, *9*, 7084–7090. [CrossRef]
9. Zheng, Y.; Jiao, Y.; Jaroniec, M.; Qiao, S.Z. Advancing the Electrochemistry of the Hydrogen−Evolution Reaction through Combining Experiment and Theory. *Angew. Chem. Int. Ed.* **2015**, *54*, 52–65. [CrossRef]
10. Eftekhari, A. Electrocatalysts for hydrogen evolution reaction. *Int. J. Hydrogen Energy* **2017**, *42*, 11053–11077. [CrossRef]
11. Wang, J.; Cui, W.; Liu, Q.; Xing, Z.; Asiri, A.M.; Sun, X. Recent Progress in Cobalt−Based Heterogeneous Catalysts for Electrochemical Water Splitting. *Adv. Mater.* **2016**, *28*, 215–230. [CrossRef] [PubMed]
12. Zhu, W.; Zhang, R.; Qu, F.; Asiri, A.M.; Sun, X. Design and Application of Foams for Electrocatalysis. *ChemCatChem* **2017**, *9*, 1721–1743. [CrossRef]
13. Hu, J.; Zhang, C.; Meng, X.; Lin, H.; Hu, C.; Long, X.; Yang, S. Hydrogen evolution electrocatalysis with binary−nonmetal transition metal compounds. *J. Mater. Chem. A* **2017**, *5*, 5995–6012. [CrossRef]
14. Li, G.; Zhang, D.; Yu, Y.; Huang, S.; Yang, W.; Cao, L. Activating MoS_2 for pH-Universal Hydrogen Evolution Catalysis. *J. Am. Chem. Soc.* **2017**, *139*, 16194–16200. [CrossRef]
15. Chen, L.X.; Chen, Z.W.; Wang, Y.; Yang, C.C.; Jiang, Q. Design of Dual-Modified MoS_2 with Nanoporous Ni and Graphene as Efficient Catalysts for the Hydrogen Evolution Reaction. *ACS Catal.* **2018**, *8*, 8107–8114. [CrossRef]

16. Luo, Z.; Ouyang, Y.; Zhang, H.; Xiao, M.; Ge, J.; Jiang, Z.; Wang, J.; Tang, D.; Cao, X.; Liu, C.; et al. Chemically activating MoS_2 via spontaneous atomic palladium interfacial doping towards efficient hydrogen evolution. *Nat. Commun.* **2018**, *9*, 2120. [CrossRef]
17. Sun, T.; Wang, J.; Chi, X.; Lin, Y.; Chen, Z.; Ling, X.; Qiu, C.; Xu, Y.; Song, L.; Chen, W.; et al. Engineering the Electronic Structure of MoS_2 Nanorods by N and Mn Dopants for Ultra-Efficient Hydrogen Production. *ACS Catal.* **2018**, *8*, 7585–7592. [CrossRef]
18. Zhang, H.; Yu, L.; Chen, T.; Zhou, W.; Lou, X.W. Surface Modulation of Hierarchical MoS_2 Nanosheets by Ni Single Atoms for Enhanced Electrocatalytic Hydrogen Evolution. *Adv. Funct. Mater.* **2018**, *28*, 1807086. [CrossRef]
19. Wan, Y.; Zhang, Z.; Xu, X.; Zhang, Z.; Li, P.; Fang, X.; Zhang, K.; Yuan, K.; Liu, K.; Ran, G.; et al. Engineering active edge sites of fractal-shaped single-layer MoS_2 catalysts for high-efficiency hydrogen evolution. *Nano Energy* **2018**, *51*, 786–792. [CrossRef]
20. Jaramillo, T.F.; Jørgensen, K.P.; Bonde, J.; Nielsen, J.H.; Horch, S.; Chorkendorff, I. Identification of active edge sites for electrochemical H2 evolution from MoS_2 nanocatalysts. *Science* **2007**, *317*, 100–102. [CrossRef]
21. Pan, H. Metal Dichalcogenides Monolayers: Novel Catalysts for Electrochemical Hydrogen Production. *Sci. Rep.* **2014**, *4*, 5348. [CrossRef]
22. Zhang, Y.; Chen, X.; Huang, Y.; Zhang, C.; Li, F.; Shu, H. The Role of Intrinsic Defects in Electrocatalytic Activity of Monolayer VS_2 Basal Planes for the Hydrogen Evolution Reaction. *J. Phys. Chem. C* **2017**, *121*, 1530–1536. [CrossRef]
23. Liang, H.; Shi, H.; Zhang, D.; Ming, F.; Wang, R.; Zhuo, J.; Wang, Z. Solution Growth of Vertical VS_2 Nanoplate Arrays for Electrocatalytic Hydrogen Evolution. *Chem. Mater.* **2016**, *28*, 5587–5591. [CrossRef]
24. Qu, Y.; Shao, M.; Shao, Y.; Yang, M.; Xu, J.; Kwok, C.T.; Shi, X.; Lu, Z.; Pan, H. Ultra-high electrocatalytic activity of VS_2 nanoflowers for efficient hydrogen evolution reaction. *J. Mater. Chem. A* **2017**, *5*, 15080–15086. [CrossRef]
25. Moutaabbid, H.; Le Godec, Y.; Taverna, D.; Baptiste, B.; Klein, Y.; Loupias, G.; Gauzzi, A. High-Pressure Control of Vanadium Self−Intercalation and Enhanced Metallic Properties in 1T-$V_{1+x}S_2$ Single Crystals. *Inorg. Chem.* **2016**, *55*, 6481–6486. [CrossRef]
26. Yang, M.; Cao, L.; Wang, Z.; Qu, Y.; Shang, C.; Guo, H.; Xiong, W.; Zhang, J.; Shi, R.; Zou, J.; et al. Vanadium self-intercalated C/$V_{1.11}S_2$ nanosheets with abundant active sites for enhanced electro-catalytic hydrogen evolution. *Electrochimi. Acta* **2019**, *300*, 208–216. [CrossRef]
27. Yang, H.G.; Sun, C.H.; Qiao, S.Z.; Zou, J.; Liu, G.; Smith, S.C.; Cheng, H.M.; Lu, G.Q. Anatase TiO_2 single crystals with a large percentage of reactive facets. *Nature* **2008**, *453*, 638. [CrossRef]
28. Mohan, P.; Yang, J.; Jena, A.; Shin, H.S. VS_2/rGO hybrid nanosheets prepared by annealing of VS_4/rGO. *J. Solid State Chem.* **2015**, *224*, 82–87. [CrossRef]
29. Chen, X.; Yu, K.; Shen, Y.; Feng, Y.; Zhu, Z. Synergistic effect of MoS_2 nanosheets and VS_2 for the hydrogen evolution reaction with enhanced humidity−sensing performance. *ACS Appl. Mater. Interfaces* **2017**, *9*, 42139–42148. [CrossRef] [PubMed]
30. Li, W.; Huang, J.; Feng, L.; Cao, L.; Liu, Y.; Pan, L. Nano-grain dependent 3D hierarchical VS_2 microrods with enhanced intercalation kinetic for sodium storage properties. *J. Power Sources* **2018**, *398*, 91–98. [CrossRef]
31. Zhang, J.; Zhang, C.; Wang, Z.; Zhu, J.; Wen, Z.; Zhao, X.; Zhang, X.; Xu, J.; Lu, Z. Synergistic Interlayer and Defect Engineering in VS_2 Nanosheets toward Efficient Electrocatalytic Hydrogen Evolution Reaction. *Small* **2018**, *14*, 1703098. [CrossRef] [PubMed]
32. Kumar, G.M.; Ilanchezhiyan, P.; Cho, H.D.; Lee, D.J.; Kim, D.Y.; Kang, T.W. Ultrathin VS_2 nanodiscs for highly stable electro catalytic hydrogen evolution reaction. *Int. J. Energ Res* **2020**, *44*, 811–820. [CrossRef]
33. Yu, S.H.; Tang, Z.; Shao, Y.; Dai, H.; Wang, H.Y.; Yan, J.; Pan, H.; Chua, D.H. In Situ Hybridizing MoS_2 Microflowers on VS_2 Microflakes in a One−Pot CVD Process for Electrolytic Hydrogen Evolution Reaction. *ACS Appl. Energy Mater.* **2019**, *2*, 5799–5808. [CrossRef]
34. Guo, T.; Song, Y.; Sun, Z.; Wu, Y.; Xia, Y.; Li, Y.; Sun, J.; Jiang, K.; Dou, S.; Sun, J. Bio-templated formation of defect-abundant VS_2 as a bifunctional material toward high-performance hydrogen evolution reactions and lithium-sulfur batteries. *J. Energy Chem.* **2020**, *42*, 34–42. [CrossRef]
35. Cao, L.; Wang, L.; Feng, L.; Kim, J.H.; Du, Y.; Yang Kou, L.D.; Huang, J. Co-N-doped single-crystal V_3S_4 nanoparticles as pH-universal electrocatalysts for enhanced hydrogen evolution reaction. *Electrochim. Acta* **2020**, *335*, 135696. [CrossRef]
36. Shi, Y.; Zhou, Y.; Yang, D.R.; Xu, W.X.; Wang, C.; Wang, F.B.; Xu, J.J.; Xia, X.H.; Chen, H.Y. Energy Level Engineering of MoS_2 by Transition-Metal Doping for Accelerating Hydrogen Evolution Reaction. *J. Am. Chem. Soc.* **2017**, *139*, 15479–15485. [CrossRef]
37. Zhang, J.; Liu, Y.; Sun, C.; Xi, P.; Peng, S.; Gao, D.; Xue, D. Accelerated Hydrogen Evolution Reaction in CoS_2 by Transition-Metal Doping. *ACS Energy Letter.* **2018**, *3*, 779–786. [CrossRef]
38. Ye, S.; Luo, F.; Zhang, Q.; Zhang, P.; Xu, T.; Wang, Q.; He, D.; Guo, L.; Zhang, Y.; He, C.; et al. Highly stable single Pt atomic sites anchored on aniline-stacked graphene for hydrogen evolution reaction. *Energy Environ. Sci.* **2019**, *12*, 1000–1007. [CrossRef]
39. Yu, J.; Guo, Y.; She, S.; Miao, S.; Ni, M.; Zhou Liu, M.W.; Shao, Z. Bigger is Surprisingly Better: Agglomerates of Larger RuP Nanoparticles Outperform Benchmark Pt Nanocatalysts for the Hydrogen Evolution Reaction. *Adv. Mater.* **2018**, *30*, 1800047–1800056. [CrossRef]
40. Qu, Y.; Pan, H.; Kwok, C.T.; Wang, Z. A first-principles study on the hydrogen evolution reaction of VS_2 nanoribbons. *Phys. Chem. Chem. Phys.* **2015**, *17*, 24820–24825. [CrossRef]
41. Liu, Y.; Liang, X.; Gu, L.; Zhang, Y.; Li, G.D.; Zou, X.; Chen, J.S. Corrosion engineering towards efficient oxygen evolution electrodes with stable catalytic activity for over 6000 hours. *Nat. Commun.* **2018**, *9*, 2609. [CrossRef] [PubMed]
42. Parishani, M.; Malekfar, R.; Bayat, A.; Gharibi, H. Hydrogen evolution reaction on VS_2-NiS_2 hybrid nanostructured electrocatalyst in acidic media: A binder-free electrode. *J. Iran. Chem. Soc.* **2022**, *19*, 4299–4307. [CrossRef]

43. Feng, T.; Ouyang, C.; Zhan, Z.; Lei, T.; Yin, P. Cobalt doping VS_2 on nickel foam as a high efficient electrocatalyst for hydrogen evolution reaction. *Int. J. Hydrogen Energy* **2022**, *47*, 10646–10653. [CrossRef]
44. Singh, V.K.; Nakate, U.T.; Bhuyan, P.; Chen, J.; Tran, D.T.; Park, S. Mo/Co doped 1T-VS_2 nanostructures as a superior bifunctional electrocatalyst for overall water splitting in alkaline media. *J. Mater. Chem. A* **2022**, *10*, 9067–9079. [CrossRef]
45. Lin, Z.; Lin, B.; Wang, Z.; Chen, S.; Wang, C.; Dong, M.; Gao, Q.; Shao, Q.; Ding, T.; Liu, H.; et al. Facile Preparation of 1T/2H $Mo(S_{1-x}Se_x)_2$ Nanoparticles for Boosting Hydrogen Evolution Reaction. *ChemCatChem* **2019**, *11*, 2217–2222. [CrossRef]